Published in final edited form as:
J Magn Reson. 2014 May ; 242: 162–168. doi:10.1016/j.jmr.2014.02.015.

Imaging of Nitroxides at 250 MHz using Rapid-Scan Electron Paramagnetic Resonance

Joshua R. Biller[a,b], **Mark Tseitlin**[a,b], **Richard W. Quine**[b,c], **George A. Rinard**[b,c], **Hilary A. Weismiller**[a,b], **Hanan Elajaili**[a,b], **Gerald M. Rosen**[d,e], **Joseph P. Y. Kao**[d,f], **Sandra S. Eaton**[a,b], and **Gareth R. Eaton**[*,a,b]

[a]Department of Chemistry and Biochemistry, University of Denver, Denver, CO 80208

[b]Center for EPR Imaging in Vivo Physiology, University of Denver, Denver, CO 80208

[c]School of Engineering and Computer Science, University of Denver, Denver, CO 80208

[d]Center for Biomedical Engineering and Technology, University of Maryland, Baltimore, Baltimore, MD 21201

[e]Department of Pharmaceutical Sciences, University of Maryland School of Pharmacy, Baltimore, Baltimore, MD 21201

[f]Department of Physiology, University of Maryland School of Pharmacy, Baltimore, Baltimore, MD, 21201

Abstract

Projections for 2D spectral-spatial images were obtained by continuous wave and rapid-scan electron paramagnetic resonance using a bimodal cross-loop resonator at 251 MHz. The phantom consisted of three 4 mm tubes containing different ^{15}N,^{2}H-substituted nitroxides. Rapid-scan and continuous wave images were obtained with 5 min total acquisition times. For comparison, images also were obtained with 29 s acquisition time for rapid scan and 15 min for continuous wave. Relative to continuous wave projections obtained for the same data acquisition time, rapid-scan projections had significantly less low-frequency noise and substantially higher signal-to-noise at higher gradients. Because of the improved image quality for the same data acquisition time, linewidths could be determined more accurately from the rapid-scan images than from the continuous wave images.

1. Introduction

Relative to other medical imaging modalities, electron paramagnetic resonance (EPR) is uniquely able to quantitatively image physiological properties including pO_2 [1–4],

---

Corresponding author: Prof. Gareth R. Eaton, Department of Chemistry and Biochemistry, University of Denver, Denver, CO 80210, Phone: 303-871-2980, Fax: 303-871-2254, geaton@du.edu.

perfusion and viability of tissues [5], pH [6–9], temperature [10], microviscosity and ease of diffusion of small molecules [11, 12], oxidative stress [13], thiol reduction [14], and thiol redox status of cells, as estimated by the ease of disulfide reduction by glutathione (GSH) in the tissue [15]. The synthetic versatility of nitroxides makes them attractive as imaging probes. For in vivo imaging, EPR in the frequency range between 250 MHz and 1 GHz is chosen because these frequencies provide sufficient depth of tissue penetration (several cm) to generate images that are not distorted by dielectric loss effects. Consequently, this paper focuses on imaging nitroxide phantoms at 250 MHz to demonstrate rapid-scan EPR methodology.

Although 300 MHz pulsed EPR imaging of nitroxides has been accomplished by the NCI group [16], the ~0.5 μs relaxation times [17] are short relative to resonator ring-down even for resonator Q of 10 to 20 at 250 to 300 MHz, which makes pulse detection challenging. We have proven the advantages of rapid scan relative to continuous wave (CW) and pulse EPR for many classes of samples, with improvements in signal-to-noise (S/N) per unit time as high as 250 [18, 19]. The electron spin relaxation times and linewidths of nitroxides [17, 20] are in the range for which rapid-scan EPR is expected to be a better imaging method than pulse or CW EPR. In this paper we show that rapid-scan imaging of a phantom composed of three different nitroxides provides better S/N per unit time than does CW imaging. We conclude that for nitroxide spin probes rapid scan is the EPR method of choice for low frequency imaging.

2. Experimental

2.1 Nitroxides and construction of phantom

^{15}N-PDT (4-oxo-2,2,6,6-tetra($^{2}H_3$)methyl-1-(3,3,5,5-$^{2}H_4$,1-^{15}N)piperidinyloxyl) with >98% isotope purity was purchased from CDN Isotopes (Quebec, Canada). ^{15}N-Proxyl (3-carboxy-2,2,5,5-tetra($^{2}H_3$)methyl-1-(2,4,4,-$^{2}H_3$,1-^{15}N)pyrrolidinyloxyl) and ^{15}N-mHCTPO (4-^{1}H-3-carbamoyl-2,2,5,5-tetra($^{2}H_3$)methyl-3-pyrrolinyloxyl) were synthesized as described in the literature [21, 22]. Quartz tubes were purchased from Wilmad Glass (Buena, NJ).

The phantom consisted of three 4.05 mm OD (2.4±0.2 mm ID) quartz tubes containing 0.5 mM aqueous solutions of ^{15}N,^{2}H-substituted-nitroxides. In addition to the aqueous solution each tube contained a one-inch long piece of 1.57 mm OD (0.97 mm ID) Teflon tubing to relieve stress on the quartz tube during the seven cycles of freeze-pump-thaw degassing that were used to deoxygenate the solutions. The Teflon tubing was distorted by the freeze-pump-thawing and was not vertical in the quartz tubes. The heights of the solutions in the 3 tubes were 1.8 cm, 2.0 cm, and 2.4 cm for ^{15}N-PDT, ^{15}N-mHCTPO, and ^{15}N-Proxyl, respectively. CW and rapid scans were recorded of the tubes individually using low incident powers and conservative modulation amplitudes for CW. Linewidths were 0.4, 0.39 and 0.25 G (1 G = 10^{-4} T) for ^{15}N-Proxyl, ^{15}N-mHCTPO and ^{15}N-PDT, respectively, and the resolved proton hyperfine splitting for mHCTPO was 0.48 ± 0.01 G, which is in good agreement with the literature [22]. In the phantom the distance between the centers of the tubes containing ^{15}N-PDT and ^{15}N-Proxyl was 8.1 mm. The total volume of solution in each tube was about 100 μL.

2.2 Spectrometer

Projections for CW and rapid-scan 2D spectral-spatial images were acquired at 251 MHz with a modified Bruker E540 console and the magnet and gradient coils described previously [23–25]. The maximum z-gradient was 8 G/cm (8×10^{-2} T/m). The original rapid-scan bridge [25] provided a maximum RF output of 50 mW. A 7 W amplifier (MiniCircuits model ZHL-03-5WF) was added to provide increased power to the resonator. The sinusoidal rapid scans were generated with a driver similar to the one described in [26], but with an additional option to trigger the digitizer once per N cycles, with N selectable between 1 and 255. This modification permits acquiring multiple scans after a single trigger. Combining the data in the multiple scans functions like a comb filter and decreases noise [19, 27–29].

2.3 Resonator design and characterization

A cross-loop resonator (CLR), which was modified from prior designs [30–32], was used for both CW and rapid-scan imaging. It consists of a 16 mm diameter by 15 mm long resonator for the sample and a larger, 25 mm diameter by 19 mm long, double saddle coil, excitation resonator (Fig. 1). The isolation between the excitation (transmit) and detection (receive) resonators was at least 60 dB. The RF shield is a rectangular solenoid of AWG 20 copper magnet wire that is coated inside with silver paint. This design allowed good penetration of the scan field without distortion, provided a good shield for the RF, and allowed the scan coils to be external to the RF shield. It reduces the rapid-scan background signal relative to resonator assemblies in which the scan coils are inside the RF shield [32].

The saddle coil arrangement (Fig. 1, bottom) allows the excitation resonator to be smaller than in parallel-coil designs [32], which increases efficiency. The saddle coils were wound using a single turn of 220/46 Litz wire. The fine wire was essentially transparent to the scanning field, thus reducing undesirable eddy current effects. The saddle coils were resonated with a common parallel capacitor, which was a 0.254 mm thick alumina substrate gold-plated on both sides, with overall dimensions of ~2 ×20 mm. A small variable capacitor was mounted in parallel with the main capacitor to allow tuning the resonant frequency to match that of the sample resonator. The Q was about 75. The B_1 field produced by the Litz wire saddle coils was perpendicular to the axis of the sample resonator. Based on comparison of power saturation curves for mHCTPO at 250 MHz and X-band [33] this resonator had an efficiency of $0.20G/\sqrt{Watt}$. It can be operated with input power as high as 1.0 Watt producing a B_1 of 0.20 G.

The sample resonator (Fig. 1) was constructed of 6 parallel, 16 mm diameter coils of 0.1 mm bare copper wire. There is a 0.8 mm gap at the top of each coil to provide for the resonator capacitor. The capacitor consists of six, 1.4 mm square, non-magnetic ceramic chip capacitors (Voltronics Inc., Salisbury, MD) with a total capacitance of 24 pF. A 0.08 mm thick substrate of Cuflon (Polyflon Corp., Norwalk, CT) with 2 parallel etches, 15 mm long and 1.2 mm wide spaced 0.8 mm apart supports the ends of the coils and the capacitors. There was a layer of 1.2 mm thick Teflon between the coils and the sample. The resonator was mounted inside a Rexolite support using Q-dope (polystyrene dissolved in acetone).

Both the excitation and sample resonators were coupled to bazooka-balun coax lines using two identical series capacitors to attain nearly critical coupling. The total capacitance was about 3 pF for the sample resonator and somewhat less for the excitation resonator. There was no coupling adjustment. In a crossed-loop resonator it is not important to have precise critical coupling, since reflected power from the excitation resonator does not reach the detector circuit. The excitation resonator coils were mounted on a Rexolite support that could be rotated to adjust the angle between the two resonator coils and thereby fine tune the isolation of the CLR.

The Q of the sample resonator containing the phantom was about 90, which is similar to that used previously for a comparison of spin echo and CW imaging of trityl radicals [34]. The active volume of the sample resonator is about 3.0 mL, so the filling factor for the solutions in the phantom is about 3%. This low filling factor is similar to what is expected when imaging a mouse tumor using the same resonator.

Rapid-scan background signals were decreased by avoiding scan frequencies that are mechanical resonances of the CLR. The mechanical resonances were characterized by two methods, which gave results that are in good agreement. Method 1 used a "chirp" pulse from 1 – 15 kHz in 35 ms. The time response to the chirped pulse was digitized and averaged about 55 times before Fourier transformation into the frequency domain (Fig. 2A). In method 2 the amplitude of the background signal was measured point-by-point at 100 Hz increments between 1 and 11 kHz (Fig. 2B). Both methods found mechanical resonances below about 2 kHz and near 5 kHz. The amplitude of the background signal was smaller at scan frequencies >~ 8 kHz, so scan frequencies > 8 kHz were used for imaging.

2.4 Rapid-scan imaging

Eighteen equally-spaced projections were recorded at $\theta = \pm 5°$to ±85° in the spectral-spatial pseudo-plane [35]. The magnetic field gradient was 8 G/cm for the projections at ±85° and decreased proportional to tan θ. The maximum gradient was selected to permit imaging one line of the ^{15}N hyperfine-split nitroxide spectrum without overlap of the second line at high gradient. In traditional spectral-spatial imaging the sweep widths are increased proportional to $1/(\cos\theta)$. Depending on the dimensions of the object, this may result in substantial regions of baseline for projections at high gradients. For the experiments reported here the sweep widths were selected to encompass the full gradient-broadened spectrum plus a modest baseline region at each end of the scan. To permit image reconstruction by filtered backprojection the high-gradient spectra were 'padded' with zeros at the low- and high-field ends to generate projections with the widths required for the spectral-spatial imaging algorithm. The magnetic field was centered on the low-field nitrogen hyperfine line. The sweep widths for the 9 projections in each quadrant were 7.2, 7.5, 7.8, 8.2, 8.8, 9.5, 10.8, 13.5, and 27.0 G. A scan frequency of 9.369 kHz was selected to avoid mechanical resonances of the CLR. The scan rate at the center of a sinusoidal scan is $a_s = \pi f_s B_m$ G s^{-1} where f_s is the scan frequency and B_m is the scan width. At the scan rates used for the imaging, the signal bandwidth is consistent with the resonator Q. As discussed below, the rapid-scan signal saturates less readily as the scan rate is increased. Projections for $\theta = \pm 5°$ to ±55° had a_s = 0.21 to 0.28 MG/s (21 to 28 T/s) so B_1 = 44 mG was used (Fig. 3). Projections for θ= ±65°, ±75°, and ±85° had a_s = 0.32 to 0.79 MG/s (32 to 79 T/s) and were acquired with B_1 = 64 mG. Signals were digitized with a Bruker Specjet II using 64k points per gradient and a 10 ns sampling interval which therefore encompassed 6.14 sinusoidal scan cycles within the digitizer time window (Supplementary Figure S1). Images were acquired with total data acquisition times of 29 s (2k averages, 1.6 s/gradient) or 5 min (22k averages, 17 s/gradient). For the '29s' image the 1 MHz filter bandwidth on the bridge output was used. For the '5 min' image a Krohn-Hite model 3955 low-pass Butterworth filter with a bandwidth set to 1.5 MHz was used on the bridge output. The absorption signals were obtained by background correction [36], sinusoidal deconvolution [37], and combination of up-field and down-field scans.

2.5 CW imaging

CW projections were obtained at the same 18 angles and magnetic field gradients as for the rapid-scan projections. The magnetic field modulation frequency was 30 kHz. The modulation amplitude was 0.5 G for θ= ±75° and ±85° and 0.2 G for other projections. To ensure that the signal was in the linear response regime B_1 = 22 mG was used (Fig. 3). The magnetic field was centered on the low-field nitrogen hyperfine line. Spectra were acquired with Bruker Xepr software and a BMC20 power supply with current control, which permits only certain values of the sweep widths. The sweep widths were 6.7 G for θ= ±5° to ±55°, 8.9 G for θ= ±65°, 11.1 G for θ= ±75°, and 24.4 G for θ= ±85°. The actual sweep widths required for filtered backprojection were obtained by interpolation and/or padding with zero's as needed. A single scan with 512 points was recorded for each projection, using a Bruker SPU digitizer. Two sets of projections were acquired with total data acquisition times of 5 or 15 min. Since the Bruker system uses an integrating digitizer, increasing scan time improves S/N. Within each data set, projections at θ= ±5° to ±65° were recorded with the same sweep time, which was increased by a factor of ~3.3 for θ= ±75°, and a factor of ~6.7 for θ= ±85°. A 3-point binomial smoothing (n=1) in Xepr was applied to the raw data as it was collected. This corresponds to about 40 mG to 140 mG smoothing for the lowest to highest gradient projections, respectively. Projections were integrated to obtain the absorption spectra that were used to generate the images.

2.6 Image reconstruction

2D spectral-spatial images (2.0 G by 2.5 cm) were reconstructed from the 18 equally-spaced projections using filtered backprojection on a 512 × 512 grid. A Gaussian filter was applied to slices through the rapid-scan and CW images after reconstruction, with full width at half amplitude corresponding to 0.6 mm in the spatial dimension and 20 mG in the spectral dimension. The linewidths of the signals were determined by least-squares fitting to spectral slices using published values of resolved and unresolved nuclear hyperfine splittings [20]. The percent RMS error was calculated for the fits to individual slices through the image. The criteria for determining the linewidth was minimization of the error for all points in the slice, including the baseline. There are systematic deviations in the linewidths toward the edges of the tubes. The scatter in the linewidth values could be decreased by manually selecting the best fit at half height but this approach would be difficult to automate, particularly in the presence of noise. This observation reinforces the importance of minimizing low frequency noise that impacts the image baseline.

3. Results and Discussion

2D spectral-spatial images of a phantom consisting of three tubes containing 0.5 mM solutions of ^{15}N,^{2}H-substituted nitroxides were obtained by CW and rapid-scan EPR for several acquisition times. The microwave powers used for the data acquisition were based on the power saturation curves in Fig. 3 for 0.25 mM ^{15}N-mHCTPO. The electron spin relaxation times for the three radicals at 250 MHz are similar and about 0.50 μs [17] for deoxygenated aqueous solutions. The linear region of the plot for the CW signals extend only to about $B_1 \sim 22$ mG, but for rapid scans the linear response region extends to B_1 about 40, 50, or 64 mG for scan rates of 0.25, 0.3 and 0.59 MG/s (25, 30, and 59 T/s), respectively. The decreased power saturation at higher scan rates is similar to what was observed previously for nitroxides at X-band [33] and is characteristic of rapid-scan EPR [18, 38].

3.1 Comparison of rapid-scan and CW images

The spatial information in EPR images is encoded with magnetic field gradients. For a distributed sample the signal broadens approximately proportional to the gradient. For the first-derivative signal that is recorded in CW EPR the amplitude decreases approximately quadratically with the increase in gradient, which makes the *S/N* substantially poorer in the higher gradient projections. These projections provide the most information about the spatial distribution of spin density. Poor *S/N* in any projection also impacts the complete image. To partially mitigate the poorer *S/N* at higher gradients the modulation amplitude was increased and more signal averaging was performed than for projections at lower gradient. The amplitude of the absorption spectrum that is recorded by rapid-scan EPR decreases approximately linearly with the increases in gradient, so the impact of high gradient on *S/N* is less severe than for CW [38]. The projections at higher gradients have wider sweep width, which makes the scan rate higher. Because of the decrease in power saturation at higher scan rate (Fig. 3), higher B_1 was used for the higher gradient rapid-scan projections. The same acquisition time was used for each of the rapid-scan projections. Rapid-scan images were obtained with 29 s and 5 min total acquisition times and CW images were obtained with 5 and 15 min total data acquisition times.

Six examples of projections obtained by rapid-scan and CW for the 5 min images are compared in Fig. 4. The CW images were reconstructed from integrals of the first-derivative CW spectra as shown in the figure. Although high-frequency noise is reduced by integration, low-frequency noise that negatively impacts baselines and lineshapes in an image is enhanced by integration [27]. At small θ (low gradient) (Fig. 4E,F) the *S/N* is good enough that projections obtained by CW and rapid-scan are quite similar, although low-frequency noise is greater for the CW projections than for the rapid-scan projections. At intermediate θ (Fig. 4C,D) noise in the CW projections is conspicuously greater than in the rapid-scan projections. At the highest θ, baseline wander and high-frequency noise is substantially greater for CW than for rapid scan (Fig. 4A,B).

Figure 5 displays 2D images of the 3-tube nitroxide phantom (Fig. 5D) reconstructed from 18 projections with a total data acquisition time of 5 min for rapid scan (Fig. 5A) or continuous wave (Fig. 5B). Also shown is a rapid-scan image with total data acquisition time of 29 s (Fig. 5C). The contours for the sample-containing regions are substantially better defined and the baselines are smoother in the 5 min rapid-scan image (Fig. 5A) than in the 5 min CW image (Fig. 5B) because of the differences in the projections as shown in Fig. 4. The contours and baseline for the 29 s rapid-scan image (Fig. 5C) are comparable to the 5 min CW image (see absorption lineshapes in Fig. 5D). The extent of the PDT signal in the spectral dimension is smaller than for Proxyl, because the PDT linewidth is narrower than the Proxyl linewidth. The spatial distribution of signal amplitude is not that of a perfect cylinder due to the presence of the deformed Teflon tube inserts. The amplitudes of the signals from mHCTPO are smaller than for PDT or Proxyl because the linewidth is relatively large and because the signal is split into a doublet with $a_H = 0.48$ G due to coupling to the ring proton. The dimensions of the tubes and spacing between the tubes in the images are in good agreement with the known dimensions (Fig. 5D). Center to center distances between tubes containing ^{15}N-Proxyl and ^{15}N-PDT in the three images are similar. For the rapid-scan images acquired in 29 s and 5 min, the distances are 7.8 and 8.2 mm, respectively. From the CW image acquired in 5 min, the distance measures 8.2 mm. The distances between tubes containing ^{15}N-Proxyl and ^{15}N-mHCTPO, and between ^{15}N-mHCTPO and ^{15}N-PDT should be ca. 4 mm which is reproduced well by rapid scan imaging in 29 s (3.9 mm/3.9 mm) or 5 min (4.4 mm/3.8 mm) and by CW imaging in 5 min (3.9 mm/3.9 mm). Based on the maximum gradient applied (8 G/cm) the theoretical spatial resolution for the narrowest-line PDT sample is ca. 0.2 mm. The inability to resolve the 0.3 mm wall thickness of the Teflon tube in each sample is attributed to the limited resolution of the image and the fact that the Teflon tubing was not vertical, which blurs its location in images with a single spatial dimension.

3.2 Lineshape parameters obtained from slices through the image

Since the goal of the imaging is to obtain spectral information as a function of position in the sample, spectral models were fit to slices through the image. The linewidths, along with the RMS errors in the fitting, are shown for the rapid-scan (Fig. 6A,C) and CW (Fig. 6B,D) images acquired in 5 min. The locations of the walls of the tube are indicated with gray dashed lines, and the black horizontal lines indicate the linewidths calculated from spectra of the tubes of the phantom measured individually. In principle the linewidths should be constant across a tube. However the small number of projections results in a 'star effect' that impacts the baselines for the images. Uncertainties in the baseline and noise in projections contribute to uncertainties in the fitted lineshapes.

For the rapid-scan image, the linewidths for ^{15}N-PDT are 0.27–0.28 G across (nearly) the entire tube, which is in reasonable agreement with the expected value of 0.25 G. The percent RMS error for the fit to each slice is ≤0.2. The linewidths for slices across the ^{15}N-mHCTPO sample vary from ca. 0.4 G on one side to 0.35 G on the other, with percent RMS error ≤0.23 for a slice in the middle of the sample, increasing to 0.27 for a slice at the edge of the sample. The linewidth fits for ^{15}N-Proxyl also have RMS errors ≤0.2, but the scatter in linewidths is larger, ca. 0.32 to 0.45 G across the sample. Of the three nitroxides in the image, ^{15}N-Proxyl has the broadest line, and its linewidths are most sensitive to baseline variations.

For the CW image the scatter in linewidths and percent RMS errors for each slice are larger than for the rapid-scan image. Both observations are attributed to the poorer baselines in the CW images. The least scatter and variation in linewidths is for ^{15}N-PDT, but the fitted linewidths for the CW image are 60% larger than the linewidth for the single tube recorded under non-line-broadening conditions. The modulation amplitude used for imaging was 0.2 G, in an effort to increase the signal to noise (*S/N*) of the CW image when acquired in the short time of 5 min. This use of modulation amplitude comparable to linewidth contributes a small amount to the broadening of the ^{15}N-PDT and ^{15}N-mHCTPO lineshapes in the CW image, but is not sufficient to explain all of the broadening. Percent RMS errors are substantially larger for the CW image slices, so there is greater uncertainty in the fit parameters. The linewidth scatter, and percent RMS error for ^{15}N-Proxyl are similar for rapid-scan and CW slices.

A major benefit of the rapid-scan technique is the ability to obtain higher *S/N* per unit time compared with CW. For comparison with the CW image acquired in 5 min, a rapid-scan image was acquired in 29 s (Fig. 5C). Linewidth and error plots are shown in Fig. S3. Decreasing the rapid-scan acquisition time by a factor of ten results in increased scatter in the fitted linewidths for all three nitroxides, although the linewidth fidelity for ^{15}N-PDT is still quite good and superior to that for the CW image collected in 5 min. The percent RMS errors for slices in the 29 s rapid-scan image are comparable to those in the 5 min CW image. The scatter in the linewidths for ^{15}N-Proxyl increased substantially to 0.15–0.5 G, reflecting the noisier background resulting from only 2k averages per projection. In the 29 s rapid-scan image the fitted linewidths in the middle of the tube for ^{15}N-mHCTPO are more uniform across the sample, but are smaller than the expected value (0.35 vs 0.39 G).

A CW image with 15 min acquisition time also was acquired, and the calculated linewidths are compared with those from the 5 min rapid-scan image in Fig. S4. The percent RMS errors are substantially lower than for the CW 5 min image, but are higher than for the 5 min rapid-scan image, particularly toward the edges of the tubes. Linewidths for the ^{15}N-PDT sample are closer to the expected value of 0.25 G, ranging from 0.25 to 0.35, but the scatter still is larger than for the 5 min rapid-scan image. The improved linewidth accuracy suggests that the major source of broadening of the ^{15}N-PDT linewidth in the 5 min CW image was due to baseline variations. Fitted linewidths for ^{15}N-mHCTPO are stable across much of the sample, and just above the expected value of 0.39 G. There is still substantial scatter (0.3–0.4 G) in the linewidths of ^{15}N-Proxyl, but the range is smaller than for the 5 min CW and rapid-scan images.

4. Conclusion

For the same data acquisition time, rapid-scan EPR provides projections with significantly improved *S/N* than CW EPR, particularly at higher magnetic field gradients. The improved *S/N* in the projections results in improved accuracy in linewidths calculated from slices through spectral-spatial images. The ability to acquire data more quickly and with improved *S/N* will facilitate in vivo applications of nitroxide imaging.

Supplementary Material

Refer to Web version on PubMed Central for supplementary material.

Acknowledgments

Partial support of this work by NIH grants NIBIB grant EB000557 (GRE and SSE), K25 EB016040 (MT), and P41 EB002034 to GMR and GRE, H. J. Halpern, PI, is gratefully acknowledged.

References

1. Elas M, Bell R, Hleihel D, Barth ED, McFaul C, Haney CR, Bielanska J, Pustelny K, Ahn K-H, Pelizzari CA, Kocherginsky M, Halpern HJ. Electron Paramagnetic Resonance Oxygen Image Hypoxic Fraction Plus Radiation Dose Strongly Correlates With Tumor Cure in FSa Fibrosarcomas. Int. J. Radiation Oncology Biol. Phys. 2008; 71:542–549.
2. Halpern HJ, Yu C, Peric M, Barth E, Grdina DJ, Teicher BA. Oxymetry deep in tissues with low-frequency electron paramagnetic resonance. Proc. Natl. Acad. Sci. U. S. 1994; 91:13047–13051.
3. Matsumoto S, Hyodo F, Subramanian S, Devasahayam N, Munasinghe J, Hyodo E, Gadisetti C, Cook JA, Mitchell JB, Krishna MC. Low-field paramagnetic resonance imaging of tumor oxygenation and glycolytic activity in mice. J. Clin. Invest. 2008; 118:1965–1973. [PubMed: 18431513]
4. Velan SS, Spencer RG, Zweier JL, Kuppusamy P. Electron paramagnetic resonance oxygen mapping (EPROM): direct visualization of oxygen concentration in tissue. Magn. Reson. Med. 2000; 43:804–809. [PubMed: 10861874]
5. Gallez B, Mader K, Swartz HM. Noninvasive measurements of the pH inside the gut by using pH-sensitive nitroxides. An in vivo ESR study. Magn. Reson. Med. 1996; 36:694–697. [PubMed: 8916019]
6. Bobko AA, Eubank TD, Voorhees JL, Efimova OV, Zweier JL, Grigor'ev IA, Samouilov A, Khramtsov VV. In vivo monitoring of pH, redox status, and glutathione using L-band EPR of assessment for therapeutic effectiveness in solid tumors. Magn. Reson. Med. 2012
7. Utsumi H, Yamada K-I, Ichikawa K, Sakai K, Kinoshita Y, Matsumoto S. Simultaneous molecular imaging of redox reactions monitored by Overhauser-enhanced MRI with ^{14}N- and ^{15}N-labeled nitroxyl radicals. Proc. Nat. Acad. Sci. U.S. 2006; 103:1463–1468.
8. Khramtsov VV, Weiner LM, Grigoriev IA, Volodarsky LB. Proton exchange in stable nitroxyl radicals. EPR study of the pH of aqueous solutions. Chem. Phys. Lett. 1982; 91:69–72.
9. Khramtsov VV, Grigor'ev IA, Foster MA, Lurie DJ, Nicholson I. Biological applications of spin pH probes. Cell. Mol. Biol. 2000; 46:1361–1374. [PubMed: 11156481]
10. Dreher MR, Elas M, Ichickawa K, Barth ED, Chilkoti A, Rosen GM, Halpern HJ, Dewhirst M. Nitroxide conjugate of a thermally responsive elastin-like polypeptide for noninvasive thermometry. Med. Phys. 2004; 31:2755–2762. [PubMed: 15543780]
11. Halpern HJ, Yu C, Peric M, Barth E, Teicher BA. Using very low frequency EPR to define bulk characteristics of pharmacologic compartments of specific tissues in vivo. Current Topics in Biophysics. 1994; 18:26–28.
12. Halpern HJ, Chandramouli GVR, Barth ED, Yu C, Peric M, Grdina DJ, Teicher BA. Diminished aqueous microviscosity of tumors in murine models measured with in vivo radiofrequency electron paramagnetic resonance. Cancer Research. 1999; 59:5836–5841. [PubMed: 10582707]
13. Elas M, Ichikawa K, Halpern HJ. Oxidative stress in live animals with techniques based on electron paramagnetic resonance. Radiat. Res. 2012; 177:514–523. [PubMed: 22348251]
14. Khramtsov VV, Yelinova VI, Glazachev YI, Reznikov VA, Zimmer G. Quantitative determination and reversible modification of thiols using imidazolidine biradical disulfide label. J. Biochem. Biophys. Methods. 1997; 35:115–128. [PubMed: 9350517]
15. Kuppusamy P, Li H, Ilangovan G, Cardounel AJ, Zweier JL, Yamanda K, Krishna MC, Mitchell JB. Noninvasive imaging of tumor redox status and its modification by tissue glutathione levels. Cancer Res. 2002; 62:307–312. [PubMed: 11782393]

16. Hyodo F, Matsumoto S, Devasahayam N, Dharmaraj C, Subramanian S, Mitchell JB, Krishna MC. Pulsed EPR imaging of nitroxides in mice. J. Magn. Reson. 2009; 197:181–185. [PubMed: 19157932]
17. Biller JR, Elajaili H, Meyer V, Rosen GM, Eaton SS, Eaton GR. Electron Spin Lattice Relaxation Mechanisms of Rapidly-Tumbling Nitroxide Radicals. J. Magn. Reson. 2013; 236:47–56. [PubMed: 24056272]
18. Mitchell DG, Tseitlin M, Quine RW, Meyer V, Newton ME, Schnegg A, George B, Eaton SS, Eaton GR. X-Band Rapid-scan EPR of Samples with Long Electron Relaxation Times: A Comparison of Continuous Wave, Pulse, and Rapid-scan EPR. Mol. Phys. 2013; 111:2664–2673.
19. Mitchell DG, Rosen GM, Tseitlin M, Symmes B, Eaton SS, Eaton GR. Use of Rapid-Scan EPR to Improve Detection Sensitivity for Spin-Trapped Radicals. Biophys. J. 2013; 105:338–342. [PubMed: 23870255]
20. Biller JR, Meyer V, Elajaili H, Rosen GM, Kao JPY, Eaton SS, Eaton GR. Relaxation Times and Line Widths of Isotopically-Substituted Nitroxides in Aqueous Solution at X-band. J. Magn. Reson. 2011; 212:370–377. [PubMed: 21843961]
21. Burks SR, Bakhshai J, Makowsky MA, Muralidharan S, Tsai P, Rosen GM, Kao JPY. ^{2}H,^{15}N-Substituted Nitroxides as Sensitive Probes for Electron Paramagnetic Resonance Imaging. J. Org. Chem. 2010; 75:6463–6467. [PubMed: 20828113]
22. Lin YJ, Teicher BA, Halpern HJ. Synthesis of 4-protio-3-carbamoyl-2,2,5,5-tetraperdeuteromethyl-3-pyrrolin-1-yloxy (mHCTPO): a selectively isotopically labeled compound for use in T_2 spin label oxymetry. J. Labelled Compds Radiopharm. 1990; 28:621–631.
23. Quine RW, Rinard GA, Eaton SS, Eaton GR. A pulsed and continuous wave 250 MHz electron paramagnetic resonance spectrometer. Magn. Reson. Engineer. 2002; 15:59–91.
24. Rinard GA, Quine RW, Eaton SS, Eaton GR, Barth ED, Pelizzari CA, Halpern HJ. Magnet and Gradient Coil System for Low-Field EPR Imaging. Magn. Reson. Engineer. 2002:51–58.
25. Quine RW, Rinard GA, Eaton SS, Eaton GR. Quantitative Rapid Scan EPR Spectroscopy at 258 MHz. J. Magn. Reson. 2010; 205:23–27. [PubMed: 20382055]
26. Quine RW, Mitchell DG, Eaton SS, Eaton GR. A Resonated Coil Driver for Rapid Scan EPR. Conc. Magn. Reson., Magn. Reson. Engineer. 2012; 41B:95–110.
27. Tseitlin M, Eaton SS, Eaton GR. Uncertainty analysis for absorption and first-derivative EPR spectra. Conc. Magn. Reson. 2012; 40A:295–305.
28. Klein MP, Barton BW. Enhancement of signal-to-noise ratio by continuous averaging: application to magnetic resonance. Rev. Sci. Instrum. 1963; 34:754–759.
29. Eaton, SS.; Quine, RW.; Tseitlin, M.; Mitchell, DG.; Rinard, GA.; Eaton, GR. Rapid Scan Electron Paramagnetic Resonance. In: Misra, SK., editor. Handbook of High Frequency EPR. Wiley; 2014.
30. Rinard GA, Quine RW, Eaton GR. An L-Band crossed-loop (bimodal) EPR resonator. J. Magn. Reson. 2000; 144:85–88. [PubMed: 10783276]
31. Rinard GA, Quine RW, Eaton GR, Eaton SS. 250 MHz crossed loop resonator for pulsed electron paramagnetic resonance. Magn. Reson. Engineer. 2002; 15:37–46.
32. Rinard GA, Quine RA, Biller JR, Eaton GR. A Wire Crossed-Loop-Resonator for Rapid Scan EPR. Concepts Magn. Reson. B, Magn. Reson. Engineer. 2010; 37B:86–91.
33. Mitchell DG, Quine RW, Tseitlin M, Eaton SS, Eaton GR. X-band Rapid-Scan EPR of Nitroxyl Radicals. J. Magn. Reson. 2012; 214:221–226. [PubMed: 22169156]
34. Epel B, Sundramoorthy SV, Barth ED, Mailer C, Halpern HJ. Comparison of 250 MHz electron spin echo and continuous wave oxygen EPR imaging methods for in vivo applications. Medical Physics. 2011; 38:2045–2052. [PubMed: 21626937]
35. Eaton GR, Eaton SS. Introduction to EPR imaging using magnetic-field gradients. Concepts Magn. Reson. 1995; 7:49–67.
36. Tseitlin M, Mitchell DG, Eaton SS, Eaton GR. Corrections for sinusoidal background and non-orthogonality of signal channels in sinusoidal rapid magnetic field scans. J. Magn. Res. 2012; 223:80–84.
37. Tseitlin M, Rinard GA, Quine RW, Eaton SS, Eaton GR. Deconvolution of Sinusoidal Rapid EPR Scans. J. Magn. Reson. 2011; 208:279–283. [PubMed: 21163677]

38. Joshi JP, Ballard JR, Rinard GA, Quine RW, Eaton SS, Eaton GR. Rapid-Scan EPR with Triangular Scans and Fourier Deconvolution to Recover the Slow-Scan Spectrum. J. Magn. Reson. 2005; 175:44–51. [PubMed: 15949747]

Research Highlights

- 2D spectral-spatial images were obtained by continuous wave and rapid-scan EPR.
- The 250 MHz bimodal cross-loop resonator had at least 60 dB isolation.
- Images obtained by rapid scan had substantially improved signal-to-noise.
- Linewidths could be determined more accurately from the rapid scan images.
- The phantom consisted of three tubes with solutions of ^{15}N,^{2}H-nitroxides.

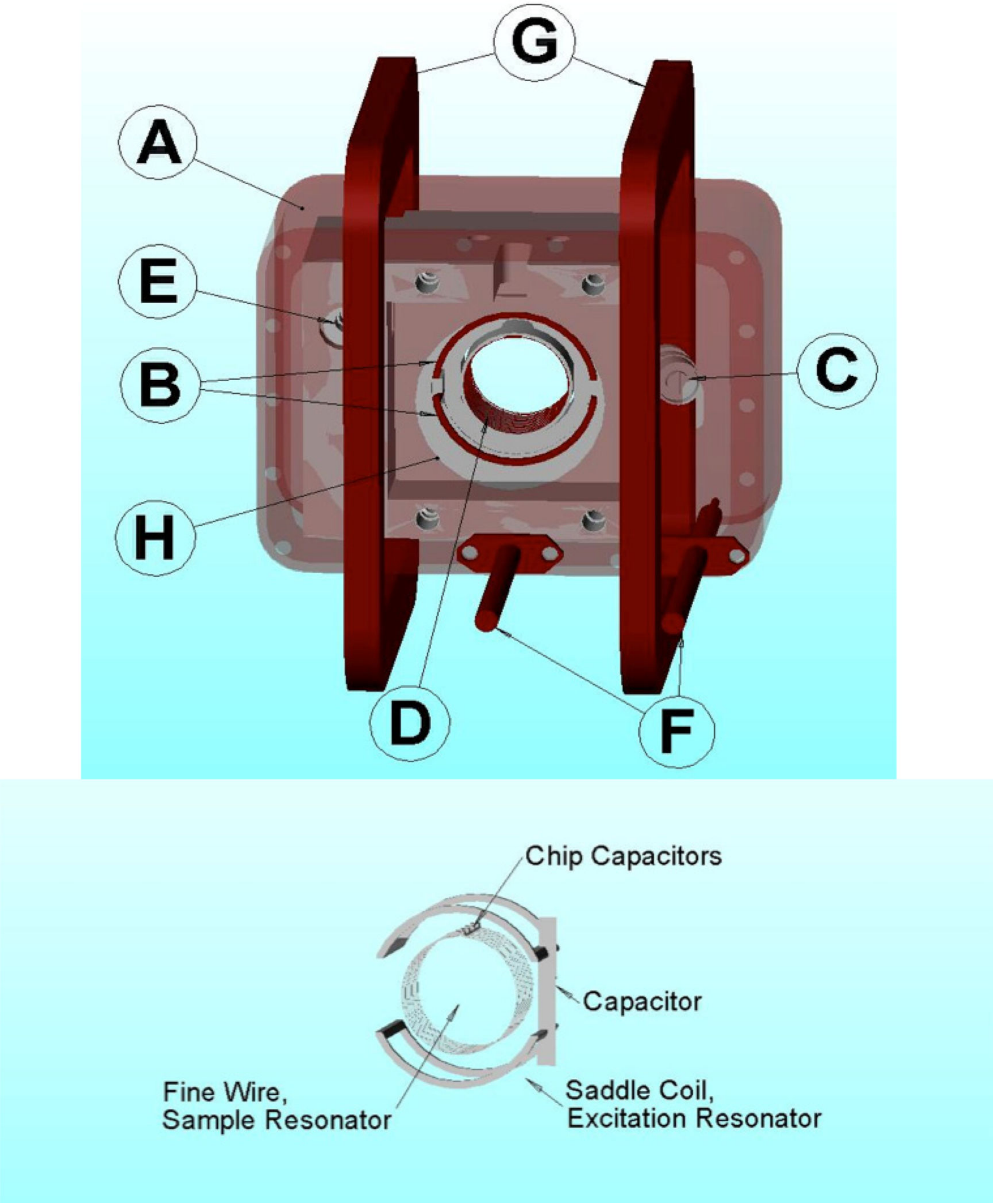

Figure 1.

Top – Cross-loop resonator assembly with scan coils: A - Wire wound RF shield; B - 25 mm saddle coil excitation resonator; C - frequency adjustment for excitation resonator; D - 16 mm fine-wire sample resonator; E - isolation adjustment; F - input and output coaxial cables; G - 89 mm square Helmholtz scan coils; H – 30 mm sample access hole in RF shield. Bottom - sketch of the resonator coils, without the shield and support structure.

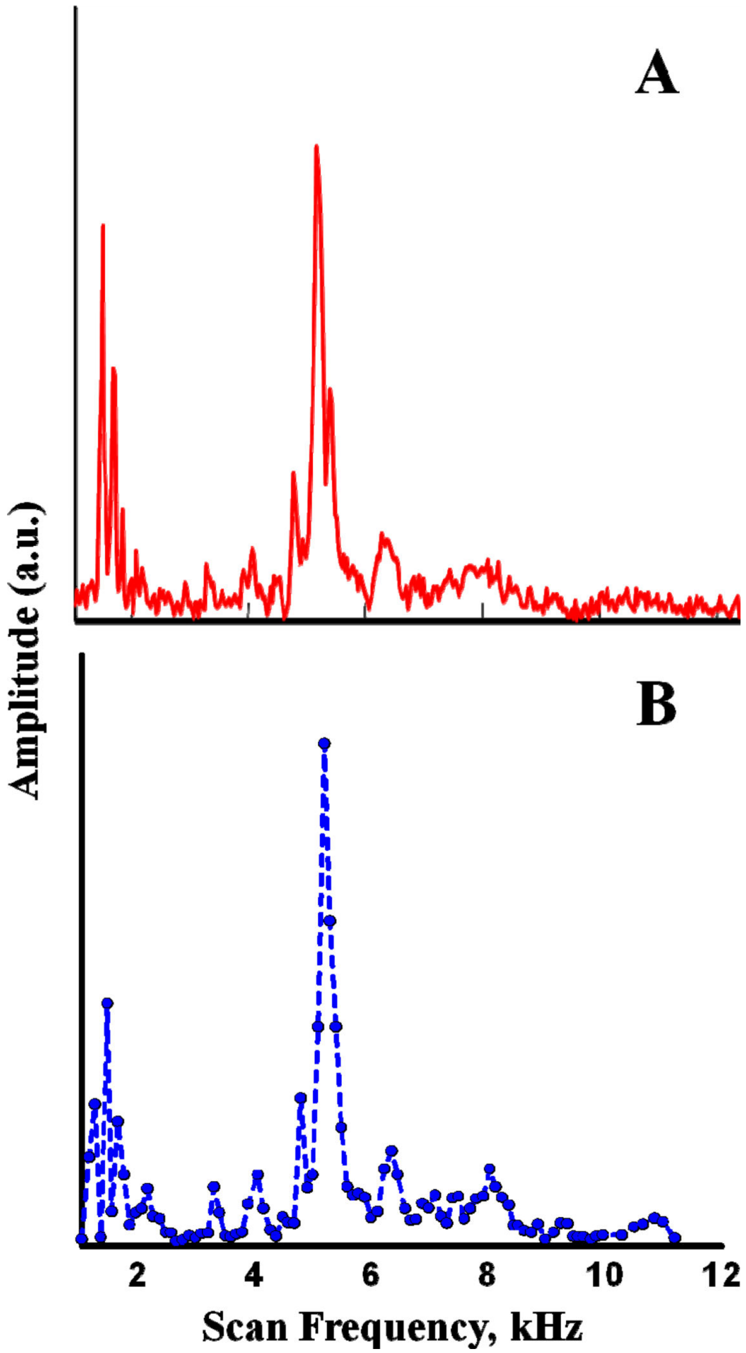

Figure 2.

Mechanical resonances of cross-loop resonator characterized by A) applying a chirp pulse from 1 – 15 kHz or (B) stepping the scan frequency and recording the rapid scan background signal. Amplitudes are in arbitrary units and are different for the two plots.

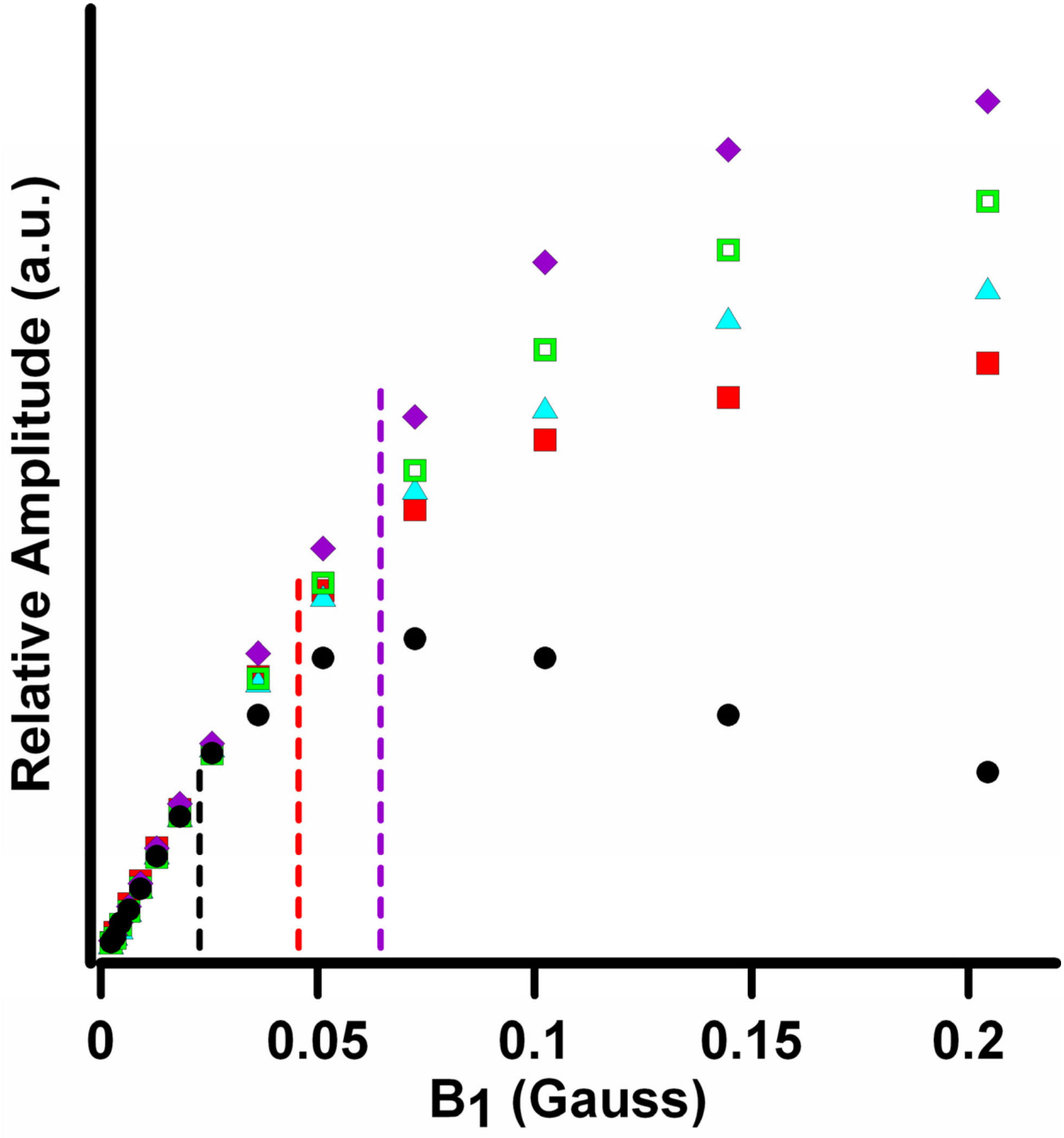

Figure 3.

Comparison of power saturation curves for 0.25 mM ^{15}N-mHCTPO in deoxygenated water in a 16 mm OD quartz tube obtained by CW (●) and sinusoidal rapid scan at 0.15 MG/s (15 T/s) (■), 0.3 MG/s (30 T/s) (▲), 0.59 MG/s (59 T/s) (□) and 0.74 MG/s (74 T/s) (◆). Amplitudes for CW spectra were peak-to-peak. Rapid scan amplitudes are calculated from spectra that had been deconvolved and background corrected. Signal amplitudes are in arbitrary units, which were scaled such that the rapid-scan signals overlay the CW data points at low power.

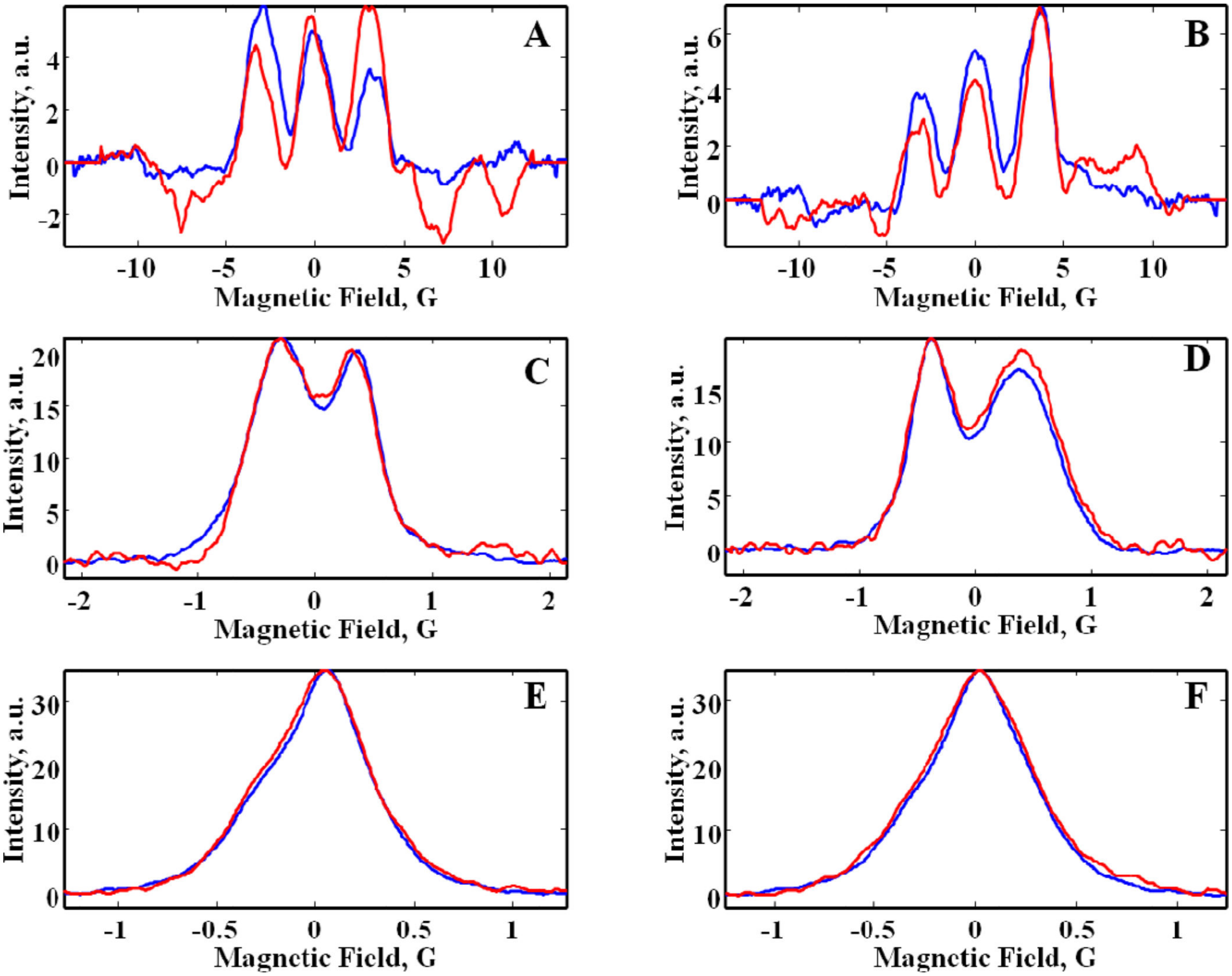

Figure 4.

Comparison of projections obtained by rapid scan (blue) and CW EPR (red) for the phantom shown in Fig. 5D at (A) θ= −85°, (B) θ= 85°, (C) θ= −55°, (D) θ= 55°, (E) θ= −5°, and (F) θ= 5° from data sets obtained with a total of 5 min acquisition time. The corresponding rapid-scan projections obtained with a total of 29 sec acquisition time are shown in Supplementary Figure S2.

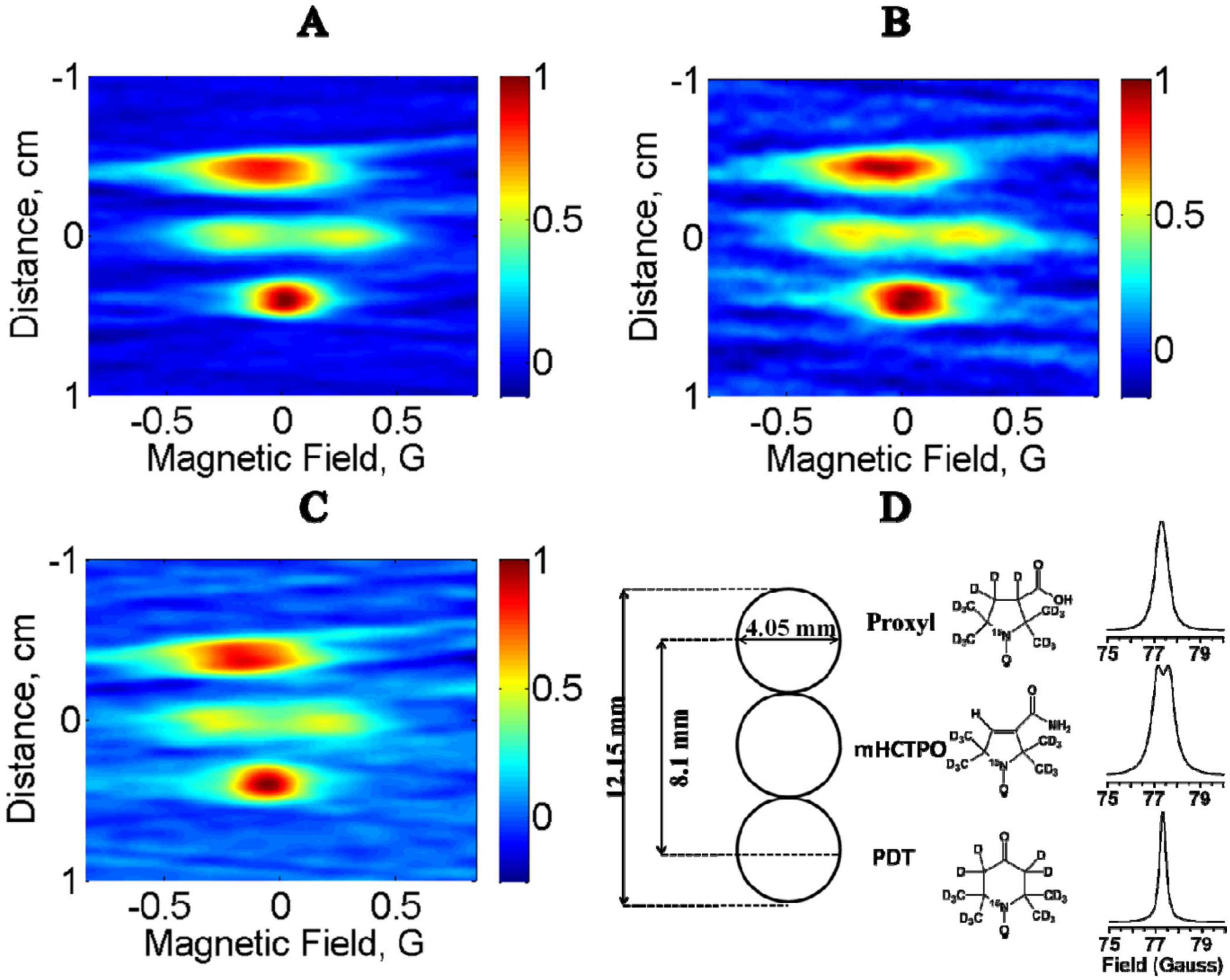

Figure 5.

Comparison of 2D spectral–spatial images reconstructed from 18 projections with a total data acquisition time of (A) 5 min for rapid scan, (B) 5 min for CW or (C) 29 s for rapid scan. (D) The phantom consisted of 3 tubes containing ^{15}N-nitroxides, aligned along the direction of the z gradient. The structures of the nitroxides and the corresponding absorption lineshapes are shown.

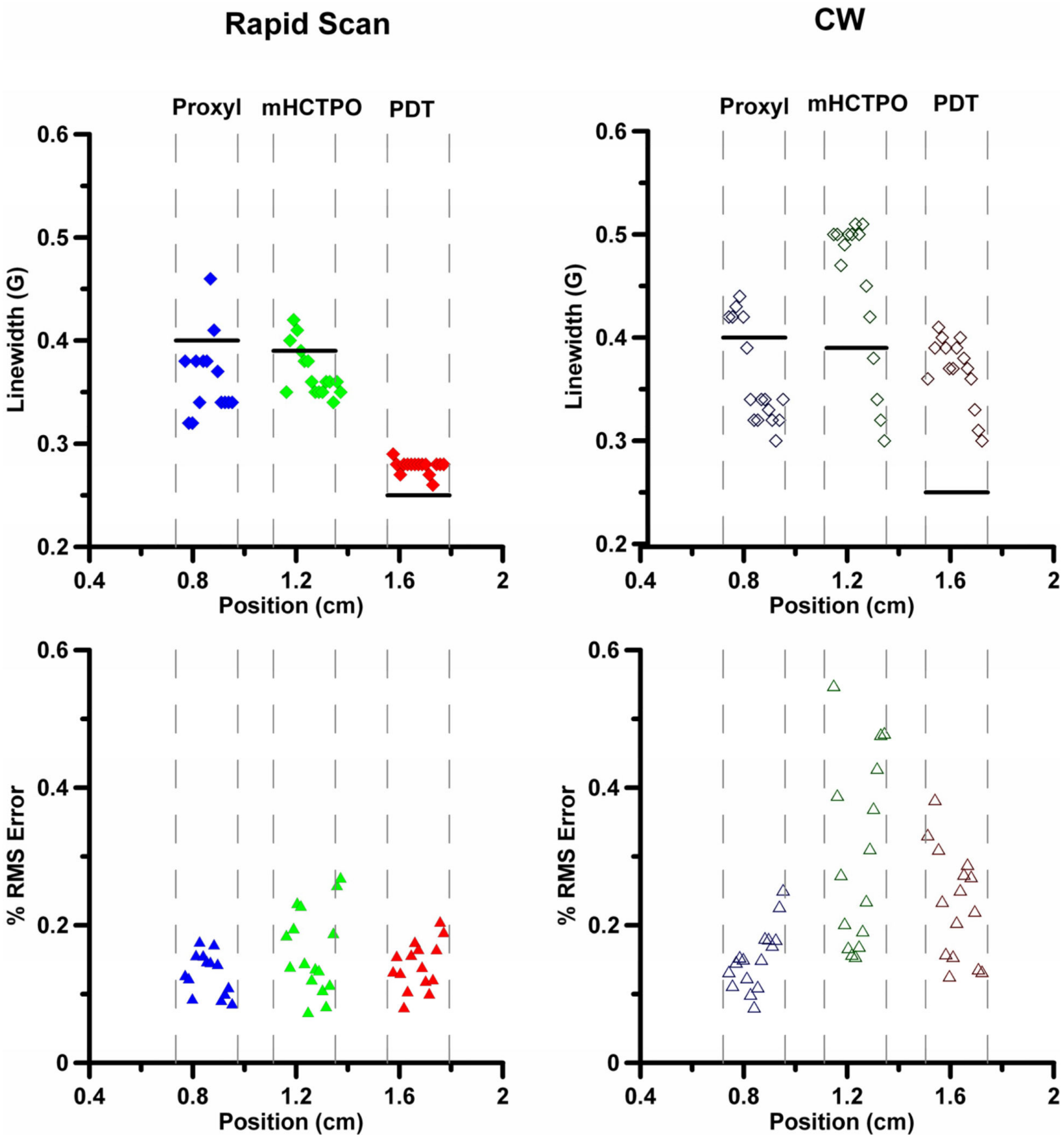

Figure 6.

Linewidths for ^{15}N-Proxyl (♦, ◊), ^{15}N-mHCTPO (◆,◊) and ^{15}N-PDT (♦, ◊) calculated by fitting spectral slices through the images obtained with a total of 5 min acquisition time and the corresponding RMS fitting errors for ^{15}N-Proxyl (▲, Δ), ^{15}N-mHCTPO (▲,Δ) and ^{15}N-PDT (▲,Δ). The RMS error is calculated for individual slices. Closed symbols designate rapid scan and open symbols designate CW. The dashed lines mark the locations of tube walls. The black horizontal lines indicate the linewidths calculated from spectra of the tubes measured individually.